

CRYSTAL ORIENTATION DEPENDENCE OF MECHANICAL AND THERMAL PROPERTIES IN FUNCTIONAL NANOMATERIALS

Atomistic Computational Analysis of the Loading Orientation-Dependent Phase Transformation in Graphite under Compression

YIPENG PENG¹ and LIMING XIONG [□] ^{1,2}

1.—Department of Aerospace Engineering, Iowa State University, Ames, IA 50011, USA. 2.—e-mail: lmxiong@iastate.edu

In this work, we perform atomistic simulations to study the phase transformations (PT) in graphite under compression. Our major findings are: (1) when the compression is parallel to the basal plane, graphite layers buckle, kink bands form, and then the diamond nucleates at the intersection of kink bands; the initially introduced dislocations block the graphite layer slippage and promote the graphite-to-diamond PT; (2) instead, when the sample is compressed normal to the basal plane, no buckling is observed, and in this situation, the pre-existing dislocations delay the structure change; and (3) the PT is found to be controlled by local stresses from which a criterion can be formulated for detecting the graphite lattice instability. Despite the limited length scales in our atomistic models, the above results may support the search for new routes to fabricate artificial diamonds at a significantly less cost than that required by traditional techniques.

INTRODUCTION

Interests in synthesizing diamonds continue since the first appearance of artificial diamonds from phase transformations (PTs) in graphite exposed to high temperature (3000 K) and high pressure (12.5 GPa) nearly 60 years ago. 1,2 In particular, because the creation of a high temperature and high pressure (HTHP) environment is extremely energydemanding, 3,4 in recent decades, intensive research has been dedicated to reducing the graphite-to-diamond PT pressure and temperature, 1,5-12 which is believed to be one key for achieving a scalable production of synthetic diamonds at the industrial scale. One popular approach to achieve this goal is using catalysts to facilitate an "easy" graphite-todiamond PT. For instance, beginning in the 1990s, the carbonates of Li and Na have been introduced as catalysts into the starting graphite in HTHP experiments, 13,14 which indeed significantly reduced the graphite-to-diamond PT pressure and temperature to a level of \sim 7.7 GPa and \sim 2000 K. However, in this approach, due to the direct contact between graphite and the catalytic metals, other forms of carbon can be formed which need to be mechanically or chemically removed from the final products,

which is not trivial. Alternatively, instead of applying hydrostatic pressure, through imposing a large plastic shear on the graphite in a rotational anvil, nanocrystalline hexagonal and cubic diamonds were obtained in a recent experiment at room temperature and a compressive stress as low as ~ 0.5 GPa. Without the need of any catalysts, this strategy is obviously very promising in facilitating an "easy" graphite-to-diamond PT at a significantly lower cost than that in HTHP, but is currently still at a "trial and error" stage because: (1) the final products from PTs in graphite under a combined compression and shear have been found to be sensitive to a variety of factors, including the loading direction, the starting graphite microstructure, the lateral confinement, the level of the applied shear strain, among many others; and (2) the role of material defects such as the grain boundaries or the plastic shear-induced dislocations in the graphite-to-diamond PT remains to be fully understood.

This has inspired a large number of computer simulations of the mechanical behavior in graphite under deformation. Historically, the continuum-level computational methods, such as finite element (FE), ^{5,15–18}, phase field, ^{19–23} or crystal plasticity models, ^{24–26} have enjoyed the most popularity.

Published online: 15 August 2019

However, such continuum-level models require constitutive rules as inputs, which are usually difficult to be accurately calibrated. In contrast, with the advent of high-performance computing, by considering materials as a collection of atoms, atomistic simulations such as molecular dynamics (MD) become a powerful tool for describing the activities of dislocations, PTs, and their interaction in materials. 27-32 In particular, for graphite, Tucker and his co-workers have performed MD simulations^{33–35} to explore its deformation behavior. They discovered that the deformation in graphite under indentation may be largely carried by a so-called "rippolocation". As far as the graphite-to-diamond PTs are concerned, Khaliullin³⁶ conducted atomic-level MD simulations using an ab initio quality neural-network potential. The pathways for the nucleation of hexagonal and cubic diamonds in graphite under compression were determined for the first time in a tiny sample containing only thousands of atoms. Furthermore, with the aim of exploring the effects of the simulation cell size, especially the dimension along the direction parallel to the basal plane, on the PT process in graphite under compression, classical MD simulations using a LCBOPII potential were conducted.³⁷ It was found that, with the increase of the simulation cell, the graphite layers first buckled before the occurrence of a PT. The buckled microstructure is related to the activities of material defects like "ripplocations" and kink bands. 33-35,38,39 Researchers believe that the graphite layer buckling, together with other pre-existing material defects (dislocations or grain boundaries), may play an important role in the graphite-to-diamond PT, although direct evidence is still lacking.

Clearly, despite extensive research in both experimental and computational aspects, fabricating diamonds through manipulating the PT in graphite still necessitates studies that can isolate the effects of a few controlling parameters, such as the loading directions and defects, on the PT process. To meet this need, here, we perform MD simulations of perfect and defected graphite samples under compression along different directions. Following this introduction, the simulation cell, boundary conditions, and the loading strategies, as well as the deployed interatomic potential, are introduced in "Computational Setup" section. The results are presented in "Simulation Results" section. "Summary and Discussion" section ends this paper with a summary of our major findings and a brief discussion of the limitations of this work together with our future endeavor along this direction.

COMPUTATIONAL SETUP

Atomistic computer models for graphite in a dimension of $5 \text{ nm} \times 68 \text{ nm} \times 83 \text{ nm}$ containing 4096,000 atoms have been constructed. The x, y, and z directions of the simulation cell are along the

 $[11\bar{2}0]$, $[1\bar{1}00]$, and [0001] directions, respectively. In order to investigate the dependence of the PT on the crystallographic orientation, the compressive loadings along two different directions are applied (Fig. 1a and b): one is along the y direction, which is parallel to the basal plane in graphite (Fig. 1a), and the other is along the z direction, i.e., normal to the basal plane in graphite (Fig. 1b). To understand the role of dislocations in graphite-to-diamond PTs, several defected graphite samples containing different numbers of dislocations have been constructed. Here, only the prismatic edge dislocations are considered, which can be initially introduced into the model through deleting a few half-graphene layers. The number of the deleted half-graphene layers is determined by the number of dislocations to be introduced. In this way, an array of the prismatic edge dislocations can be generated. Figure 1c shows a typical defected graphite sample containing nine dislocations, which are initially introduced into the sample with uniform spacing between each other. Thereafter, before applying the compressive loading, with a time step of 0.5 fs, both the perfect and the defected graphite samples are equilibrated at T = 2000 K in NPT ensembles for 20 ps. During the equilibration, the pressure components along the lateral direction, i.e., P_x and P_y , are set at zero, and P_z is set at 30 GPa. Such a "precompression" along the normal direction of the basal plane is used to reduce the graphitic layer spacing from 3.35 Å to 2.42 Å, which will significantly speed up the onset of the PTs in graphite under compression. During all the above equilibrations, periodic boundary conditions (PBCs) are applied along the *x*, y, and z directions. To ensure that the atomic configuration obtained through this equilibration is in equilibrium, we measure the local stress near the equilibrated dislocation core at 0 K and compare it with the solution from elasticity marked by the black lines and labels in Fig. 1d and e. Here, the atomic stress is calculated using the Virial stress formula for simplicity, which has been implemented in LAMMPS, 40 although the consistency between the Virial stress formula and the concept of a Cauchy stress is still in debate. 41-44

After the equilibration, the samples are compressed along the y and z directions at a constant loading speed of 100 m/s in an NVT ensemble at T = 2000 K. During the compression, the PBCs are always maintained along the non-compressed directions, while a non-periodic and shrink-wrapped boundary is applied along the loading direction. That is, when the sample is compressed along the v direction, the PBCs are imposed along the x and z directions. Instead, when the sample is compressed along the z direction, the PBCs are imposed along the x and y directions. At both the equilibration and compressive loading stages, a bond order empirical potential, LCBOP, 45 for describing the atomic interactions in graphite is chosen because, firstly, it includes a dihedral term together with a term for

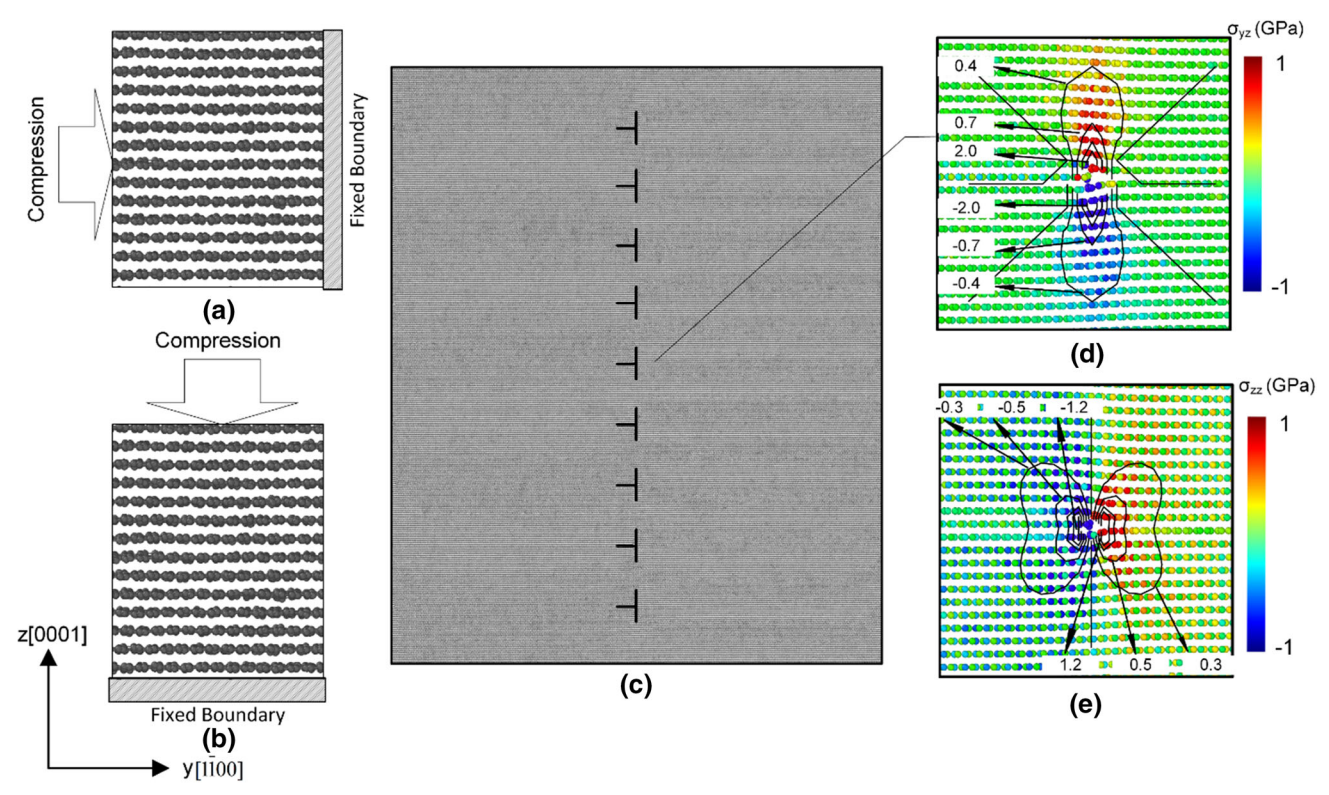


Fig. 1. Atomistic computer models for graphite samples under compression along a direction that is (a) parallel and (b) normal to the basal plane; (c) a defected sample containing an array of built-in prismatic edge dislocations; (d) the shear (σ_{yz}) and (e) the normal stress (σ_{zz}) near a dislocation core and its comparison with that calculated by elasticity.

the long-range van der Waals interactions between the graphitic layers. Those two terms are absent in many other potentials, such as Tersoff, 46-49 for carbon materials, but can be very important for correctly reproducing the stacking sequences of graphite layers, especially in defected samples where the stacking sequences deviate from the perfect ones. 50,51 This feature facilitates its applicability for capturing the graphite layer stacking sequence changes during a graphite-to-diamond PT process. Secondly, it can approximately capture the sp²-bond breaking and also the sp³-bond formation involved in a graphite-to-diamond PT process, although in an empirical manner. Thirdly, compared with other high-fidelity potentials, such as COMB3⁵² and ReaxFF,⁵³ it is significantly less demanding in computational resource. This enables us to explore the effects of the sample sizes on the PT process in relatively larger material specimens.

SIMULATION RESULTS

PTs in perfect and defected graphite under compression along the y [1100] direction

When a graphite sample is compressed along the y direction, we found that, if the applied compressive strain is sufficiently small (less than 0.02, prior to the initiation of buckling as shown in the first row of Fig. 2), the graphite layers remain flat and the deformation at this stage can be fully recoverable when unloading. Thereafter, with a further increase of the compressive stress, the materials start to yield locally. Figure 2 presents the snapshots of the atomic structure evolution near a region where the permanent deformation occurs in perfect and defected graphite samples. In order to quantify the local material deformation, using the initial atomic configuration in the zero-strained sample as a reference, an atomic-level Von-Mises shear strain^{54,55} is calculated and used to color the atoms in OVITO⁵⁶ in Fig. 2:

$$\eta_i^{\text{Mises}} = \sqrt{\eta_{yz}^2 + \eta_{xz}^2 + \eta_{xy}^2 + \frac{(\eta_{yy} - \eta_{zz})^2 + (\eta_{xx} - \eta_{zz})^2 + (\eta_{xx} - \eta_{yy})^2}{6}}$$
(1)

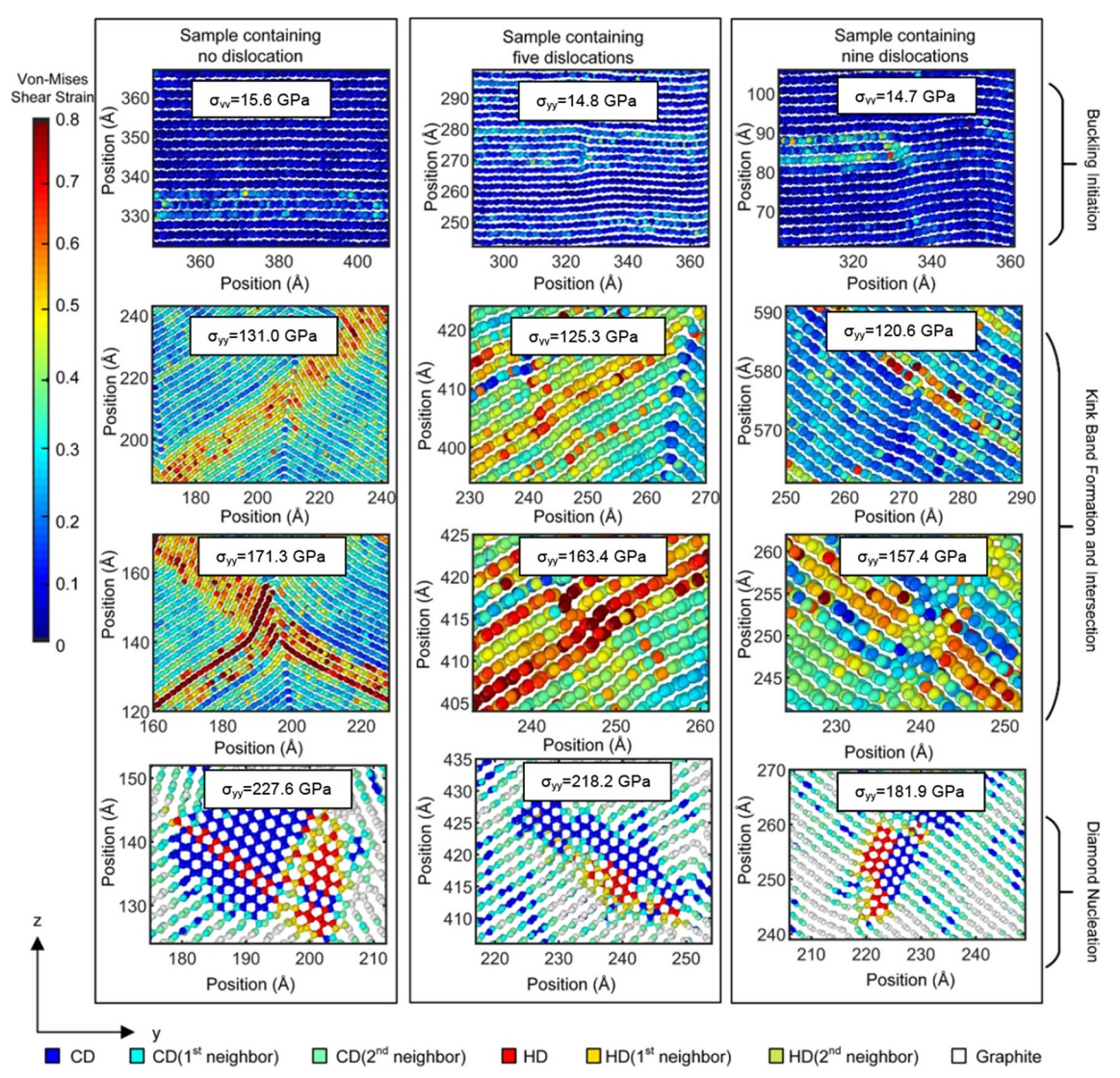


Fig. 2. Time sequences of the snapshots of the deformation behavior in perfect and defected graphite containing five and nine dislocations when the compressive loading is applied along the *y* direction. The buckling of graphite layers and their slippage with each other are visualized through the atomic-level Von-Mises shear strain, which is calculated using the initial atomic configuration as a reference. The *labels* on the *axes* in these images indicate the actual positions. *CD* and *HD* represent cubic diamond and hexagonal diamond, respectively.

where η_{ij} (I = x, y, and z; j = x, y, and z) are the components of a Green-Lagrangian strain tensor on each atom. 50,51 It is clearly seen that, when the graphite samples are deformed by a compressive loading along a direction parallel to the basal plane, the deformation behavior in both perfect and defected graphite samples containing either five or nine dislocations falls into three characteristic stages: (1) a few graphite layers start to buckle at a critical compressive stress of σ_Y , the values of σ_Y are 39.55 GPa, 35.51 GPa, and 32.81 GPa for the perfect sample, the defected sample containing five dislocations and the one containing nine dislocations, respectively; (2) multiple graphite layers are collectively buckled with the continuous increase of the loading, kink bands start to form (the bands can be clearly identified as a collection of those atoms in

red, as shown in the second row in Fig. 2), and upon further compression, many kink bands are formed and eventually intersect with each other; and (3) the intersections of those kink bands "block and jam" the slippage of the graphite layers, introduce high local stress–strain concentrations, and, in turn, activate the nucleation and growth of diamond crystals, which are recognized using "Identify the diamond structure" in OVITO. Despite the commonality in terms of the above three-stage deformation process, the critical stress, σ_{yy-C} , for nucleating diamonds in perfect and defected graphite samples are obviously different: the more dislocations, the less compressive stress required to active a graphite-to-diamond PT.

The effects of dislocations on the graphite-todiamond PT can be quantified through correlating

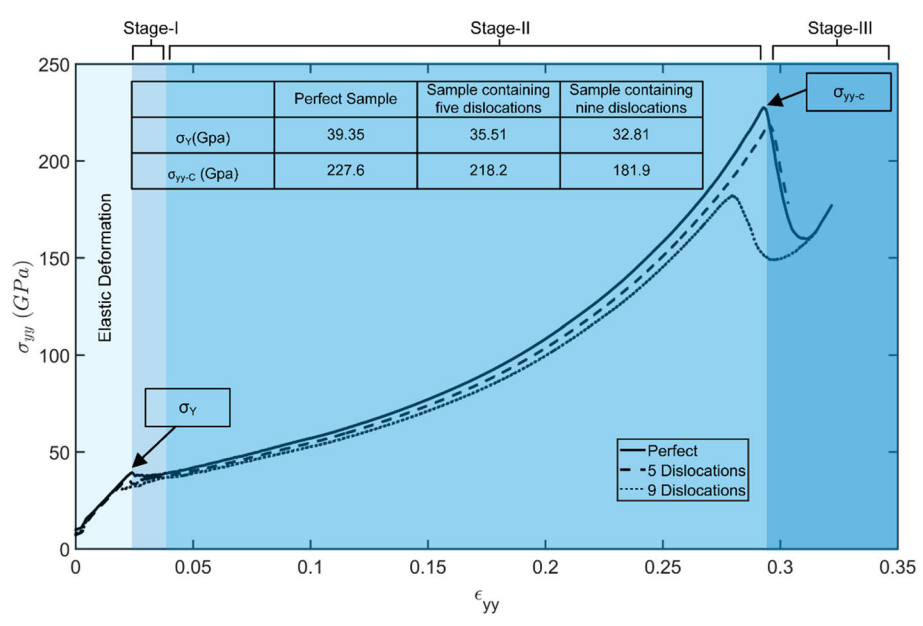


Fig. 3. Stress–strain curves in perfect and defected graphite under compression along the y [1 $\bar{1}$ 00] direction: the three-stage deformation in a perfect sample are *shaded* as *Stages-I*, -II, and -III; the critical stresses are also indicated.

the number of dislocations with the reduction of the critical compressive stress. Here, we measure the averaged stresses in perfect and defected samples along the loading direction, i.e., σ_{yy} , and plot it against the applied compressive strain (Fig. 3). It can be seen that, when the compressive strain is small, all the samples are under elastic deformation. At this stage, the stress-strain curves are linear and overlap with each other, from which Young's modulus can be approximately measured as 1226 GPa. This is larger than the experimentally measured elastic constant (1060 GPa) of graphite along a direction parallel to the basal plane, ⁵⁸ but is reasonably acceptable due to the small sample sizes and the idealized crystalline structure in the simulation cell. Thereafter, in parallel to the threestage deformation process observed in Fig. 2, the stress-strain curves in Fig. 3 are seen to also fall into three regimes: (1) when the applied stress approaches a level of σ_V as indicated in Fig. 3, the materials yield, corresponding to the Stage-I deformation at which a few graphite layers start to buckle; (2) at Stage-II, multiple graphite layers buckle, and kink bands form and interlock with each other; correspondingly, the stress exponentially increases with the increase of the applied compressive strain; and (3) at Stage-III, due to the nucleation and growth of the diamond crystal at the intersection of kink bands, a sudden drop in the stress-strain curve is observed. Obviously, there exists a perfect correspondence between the stressstrain curves and the three-stage deformation process. From Fig. 3, for graphite under compression along the y direction, the critical compressive stress, σ_{vv-C} , required for the occurrence of PTs can be measured. The obtained results are summarized in the inset table in Fig. 3. The reduction of

graphite-to-diamond PT stress can be quantitatively correlated with the number of dislocations in the starting materials. In details, when nine dislocations are introduced into the models, the critical compressive stress for the occurrence of PT reduces from $\sim\!228$ GPa to 182 GPa, which corresponds to a $\sim\!20\%$ reduction and suggests the possibility of a dislocation-assisted PT.

Since the present atomistic simulation provides us with the capability of tracking the motion of individual atoms, here we attempt to identify the roles of dislocations through analyzing the process of the diamond nucleation as a consequence of the change in the graphite layer stacking sequences accompanied by an atomic-level buckling out of the basal plane. For graphite under no deformation, Fig. 4a shows the structure of hexagonal graphite (HG), a typical "ABA" stacking sequence of graphite layers. When hexagonal graphite containing no defects is compressed along the y direction (Fig. 4b), the graphite layers buckle and the slippage between them is blocked by the sharp angle vertex of the buckling. This, in turn, leads to the stacking sequence change from "ABA" to "AAA", which corresponds to orthorhombic graphite (OG). With further increase of the compressive loading, the local buckling occurs within the newly formed OG layers and activates hexagonal diamond (HD) nucleation and growth (Fig. 4b). In contrast, for defected graphite containing dislocations, prior to the formation of the sharp buckling vertex angles, the initially introduced dislocations can effectively block the slippage of graphite layers. Thereafter, with a small increase of the compressive strain, nearby the dislocation core, the hexagonal graphite in "ABA" stacking sequences can be easily trans-"ABC", formed to which corresponds

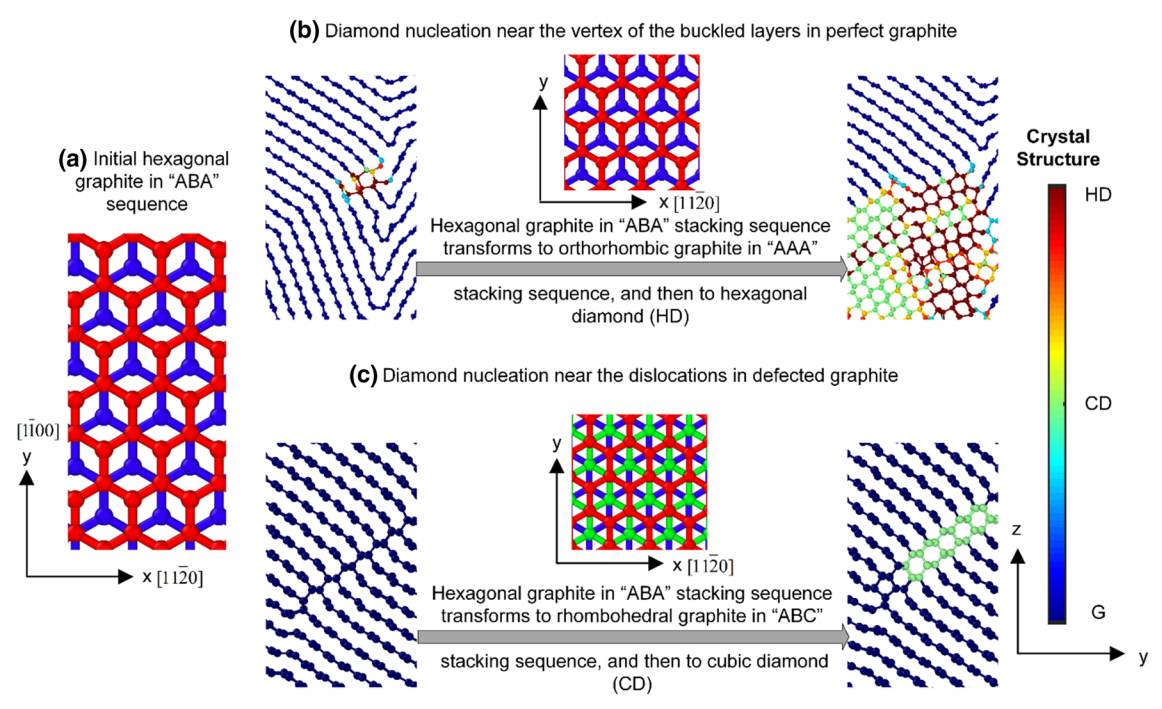


Fig. 4. A detailed analysis of the evolution of the graphite layers stacking sequence change and the resulting graphite-to-diamond PTs in perfect and defected graphite under a compressive loading along the y direction: (a) the "ABA" stacking sequence in un-deformed hexagonal graphite; (b) the process of PT from hexagonal graphite to hexagonal diamond (HG \rightarrow OG \rightarrow HD); and (c) the process of a dislocation-assisted PT from hexagonal graphite to cubic diamond (HG \rightarrow RG \rightarrow CD).

rhombohedral graphite (RG) and then to the cubic diamond (CD). The above findings suggest two totally different PT pathways for diamond nucleation in perfect and defected graphite when compressed along the y direction: $HG \rightarrow OG \rightarrow HD$ in perfect graphite and $HG \rightarrow RG \rightarrow CD$ near a dislocation in defected graphite. However, it should be pointed out that, at a later stage of the deformation, these two pathways appear in both perfect and defected samples. Hence, no matter whether or not the starting graphite sample contains dislocations, if the graphite is compressed along the y direction, the CD and HD coexist in the resulting final products.

The above analysis also suggests that, in both perfect and defected graphite under deformation, diamond nucleation necessitates at least three local structure changes: (1) a deviation of the graphite layer stacking sequence from that in HG; (2) a blockage of any further graphite layer slippage with each other, either by sharp buckling angle vertex (Fig. 4b) or by dislocations (Fig. 4c); and (3) an atomic-level buckling of the graphite layer out of the basal plane for triggering the formation of sp³ bonds between the layers. Then, we characterize the local stress states at 16 potential diamond nucleation sites to investigate the parameter that controls the local structure changes. It goes through the following three steps: (1) the volume elements in a dimension of 3 nm \times 3 nm \times 3 nm are constructed around each potential diamond nucleation site; (2) the six components of the local stresses on the volume elements associated with each nucleation site are calculated using the Virial stress formula; and (3) the principal stresses, σ_{I} , σ_{II} , and σ_{III} , at each nucleation site are calculated. The obtained data are then plotted in the $\sigma_{I} - \sigma_{II} - \sigma_{III}$ coordinate system (Fig. 5a). The projections of those data onto the $\sigma_{I} - \sigma_{III}$ and the $\sigma_{II} - \sigma_{III}$ planes are also provided in Fig. 5b and c, respectively. Surprisingly, all the principal stress states at different potential diamond nucleation sites fall approximately into one plane, expressed mathematically as Eq. (2).

$$0.151 * \sigma_I + 0.1044 * \sigma_{II} + \sigma_{III} = 264 \text{ GPa}$$
 (2)

Therefore, we conclude: (1) the local structure changes are controlled by local principal stresses, and (2) all the six components of the local stress tensor contribute to the structure changes. Furthermore, Eq. (2) may be used in higher length-scale computer models, such as FE, $^{5,15-18}$ or phase field models, $^{19-23,59}$ to detect the diamond nucleation in graphite under compression along the y direction.

PTs in perfect and defected graphite under compression along the z [0001] direction

Due to its highly anisotropic crystalline structure 60 (1020 GPa for the planar Young's modulus, while 37 GPa along the c-axis direction), graphite under compression along the direction normal to the basal plane can behave significantly different from that under compression parallel to the basal plane. Figure 6 presents the snapshots of the deformation

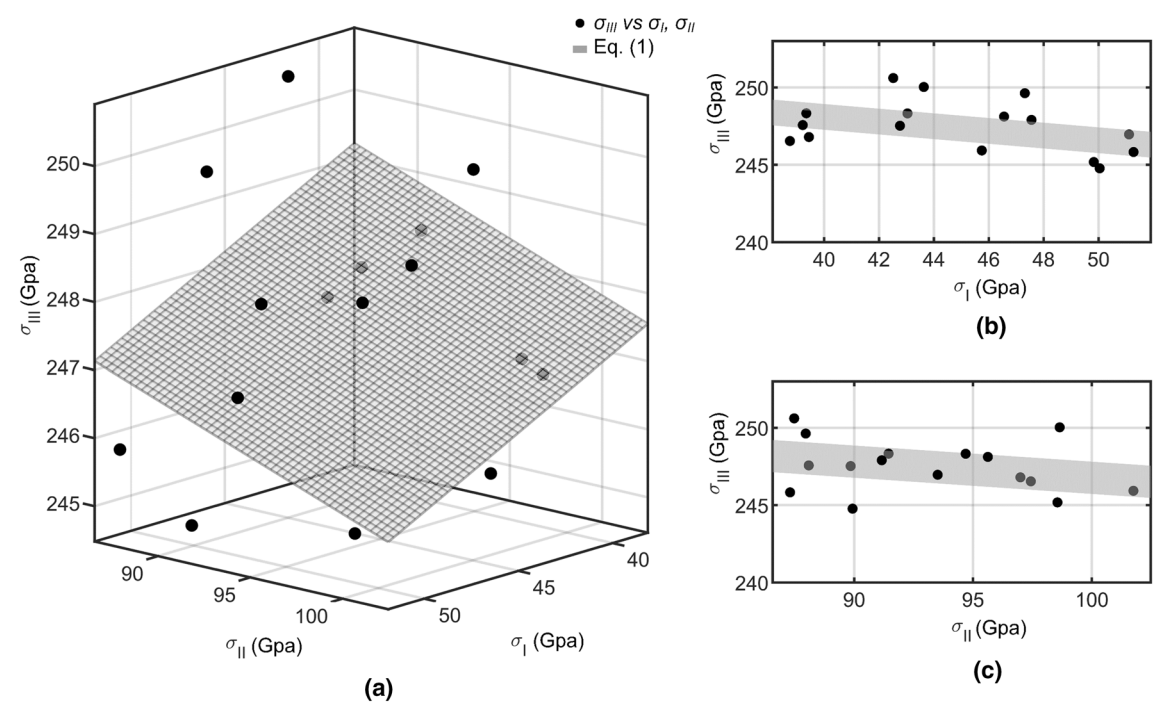


Fig. 5. The principal stresses, σ_{l} , σ_{ll} , and σ_{ll} , calculated from the local stress states in 16 different sites for potential diamond nucleation in graphite under compression along the y direction: (a) the stress states in those 16 diamond nucleate sites fall into a plane in the principal stress ($\sigma_{\Gamma}\sigma_{ll}\sigma_{ll}$) space coordinate system; (b) the projection of the stress states onto the $\sigma_{\Gamma}\sigma_{ll}$ plane; and (c) the projection of the stress states onto the $\sigma_{ll}\sigma_{ll}$ plane.

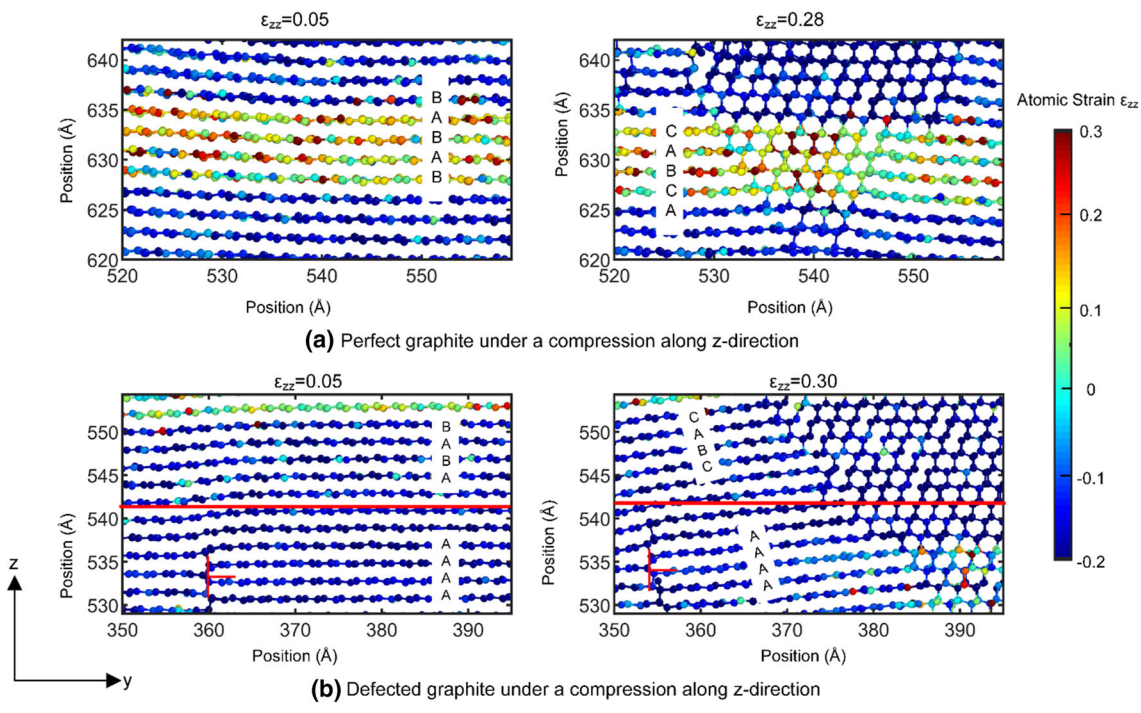


Fig. 6. The snapshots of the PTs in perfect and defected graphite under compression along the z direction: (a) in a perfect sample containing no defects, the graphite layer stacking sequence changes from "ABA" to "ABC" when $\varepsilon=0.05$ and then diamond nucleates near the boundaries when $\varepsilon=0.28$; (b) in a defected sample containing five dislocations, the graphite layer stacking sequence changes from "ABA" to "ABC" underneath the compressed sample boundaries, but is blocked by the initially introduced prismatic dislocations; and then the diamond also nucleates near the boundaries at a strain of $\varepsilon=0.30$.

behavior in perfect and defected graphite under compression along the z direction, i.e., the normal direction of the basal plane in graphitic materials. It differs from the structural evolutions in Fig. 2 for graphite under compression along the y direction in the following four main aspects: (1) when the loading is normal to the basal plane, even at a very high level of compressive strain, in both perfect and defected samples, the graphite layers always only get closer with each other and never buckle, while the graphite layers can be easily buckled when the compression is along the y direction; (2) the change of the graphite layer stacking sequence in Fig. 6 only occurs near the sample boundaries where the loading is applied; instead, the stacking sequence change can take place anywhere in the whole sample when the slippage between graphite layers is blocked or altered by the presence of the sharp angle vertex of a buckling for graphite under compression along the y direction; (3) no matter whether the starting sample contains dislocations or not, when compressed along the z direction, the graphite layers stacking sequence always only transforms from "ABA" to "ABC" (Fig. 6b), and in contrast, when the compression is along the y direction, the stacking sequence changes from "ABA" to "AAA" and "ABC" respectively; and (4) as a consequence of the dominating stacking sequence change is "ABA" \rightarrow "ABC" near the sample boundaries, diamond nucleates underneath the loading zone (Fig. 6a, b), the newly formed diamonds are mainly in cubic structure. In contrast, hexagonal and cubic diamonds co-exist in the final products from the compression of the graphite along the y direction.

More interestingly, for the defected graphite under compression along the *z* direction, the initially introduced prismatic dislocations can actually

block the propagation of the graphite layer stacking sequence change. In details, as shown in Fig. 6b, at a compressive strain of $\varepsilon = 0.05$, the stacking sequence of the graphite layers above the dislocations (the material domain above the red line in Fig. 6b) has changed to "ABC" but does not transform to "ABC" in those layers where the dislocation sits. For the sample containing no dislocations (Fig. 6a), at this strain level, the stacking sequence of all the graphite layers has transformed to "ABC" and is ready for the nucleation of cubic diamonds through a route of HG \rightarrow RG \rightarrow CD. In that sense, we believe that prismatic dislocations only assist the PTs when the compressive loading is parallel to the basal plane in graphitic materials, and they may delay or even suppress the occurrence of PTs in graphite when the compressive loading is along the *z* direction. This can be confirmed through the following constitutive response of a defected graphite to the compression along the z direction and its comparison with that of a perfect sample.

Figure 7 shows the stress–strain curves of the perfect and defected graphite (containing five initially built-in prismatic dislocations) under compression along the z direction. The critical compressive stress at which the diamond starts to nucleate are indicated as σ_{zz-C} . Obviously, the activation of a graphite-to-diamond PT in the defected graphite requires noticeably larger stress than that by the perfect sample: the critical compressive stress under which the PT occurs in the perfect sample is 187 GPa, and is 204 GPa in the defected sample, respectively. This result implies that (1) material defects not always promote the PTs, and (2) the interplay between dislocations and PTs in graphite largely depends on the direction of the applied loadings. Also, similar to the previously discussed PT behavior in graphite

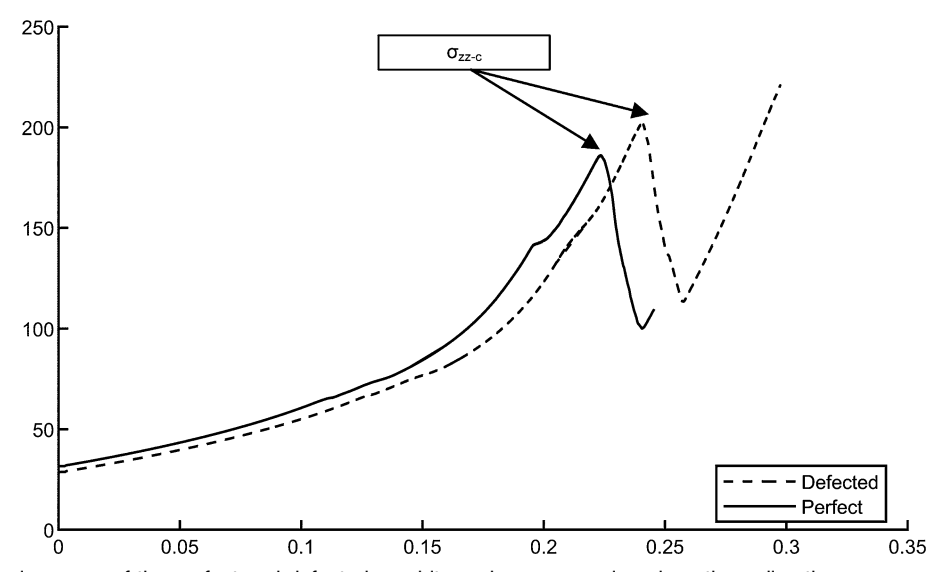


Fig. 7. The stress–strain curves of the perfect and defected graphite under compression along the z direction..

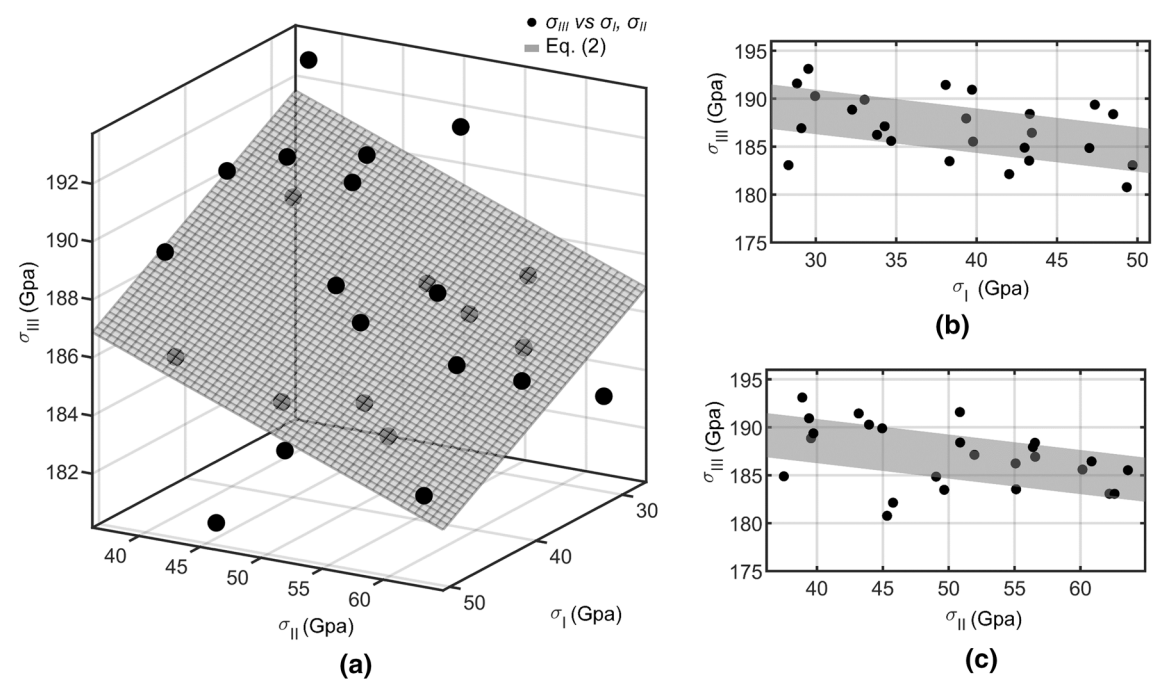


Fig. 8. The principal stresses, σ_{II} , σ_{II} , and σ_{IIII} , calculated from the local stress states in 20 different diamond nucleation sites in graphite under compression along the z direction: (a) the stress states in those 20 diamond nucleate sites fall into a plane in the principal stress ($\sigma_{I} - \sigma_{III} - \sigma_{III}$) space coordinate system; (b) the projection of the stress states onto the $\sigma_{I} - \sigma_{III}$ plane; and (c) the projection of the stress states onto the $\sigma_{II} - \sigma_{III}$ plane.

compression along the y direction, after the stacking sequence change from "ABA" to "ABC", the diamond may nucleate simultaneously at multiple atomic sites near the sample boundary. Those potential nucleation events are found to be triggered by lattice stability, i.e., the atomic-level buckling of graphite out of the basal plane, which is believed to be controlled by the local stress states. Follow the same procedure in the previous section, here we measure the full stress tensor around each potential diamond nucleation site, calculate the principal stresses, σ_{I} , σ_{II} , and σ_{III} , and plot them in the principal stress coordinate system (Fig. 8a). The projections of these data points on the $\sigma_I - \sigma_{III}$ and the $\sigma_{II} - \sigma_{III}$ are provided in Fig. 8b and c, respectively. Again, similar to that in Fig. 5a-c, results in Fig. 8a-c show that the principal stress states at different potential diamond nucleation sites fall into one plane, which can be fitted as the Eq. (3). It may be used as a criterion for detecting the lattice instability in continuum-level models for simulating the deformation behavior in graphite under compression along the z direction.

$$0.1956\sigma_I + 0.1615\sigma_{II} + \sigma_{III} = 202 \text{ GPa}$$
 (3)

SUMMARY AND DISCUSSION

To summarize, in this work, we have carried out MD simulations to investigate the phase transformation (PT) behavior in perfect and defected single-crystalline graphite under a compressive loading along different directions. The results show that the

conditions required for the occurrence of graphite-to-diamond PT, the atomistic mechanisms responsible for the PT processes, and the microstructure of the products resulting from the PT, can all be largely determined by the loading direction and the initially introduced material defects. Several major findings can be highlighted as:

- (1) When the compressive loading is parallel to the basal plane, the graphite layers always buckle first, and kink bands form. And then, at the intersection of the kink bands, diamonds nucleate through either an HG \rightarrow OG \rightarrow HD or an HG \rightarrow RG \rightarrow CD process. In this situation, at the kink band intersections, the initially introduced prismatic dislocations are found to promote the PT through "jamming" the slippage between graphite layers;
- (2) For the graphite sample under compression along a direction normal to the basal plane, the wavy graphite layer buckling is not observed and no kink band is formed. The stacking sequence between the graphite layers is found to change from "ABA" to "ABC", diamond nucleates underneath the boundary where the compressive loading is applied, and then cubic diamonds are formed. In this scenario, the initially introduced prismatic dislocations are found to suppress the graphite-to-diamond PT through delaying the graphite layer sequence change from "ABA" to "ABC";
- (3) No matter the graphite is compressed parallel or normal to the basal plane, when diamonds starts to nucleate, it may occur at multiple different sites.

The local stress states around these potential nucleation sites are found to fall into one plane in the principal stress space. This suggests that all the six components of the local stress tensor contribute to the crystal structure change. A mathematical functional form of this plane fitted from MD data may be used in formulating a criterion for detecting the stress-controlled lattice instability induced by the PTs in graphite under deformation.

Although the above results may find applications in interpreting experimental observations, supporting the development of higher length-scale computer models, and even suggesting new routes for synthesizing diamonds from graphite, great care needs to be taken due to several limitations of the present work. Firstly, for the LCBOP potential employed here, the ${\rm sp}^2$ bonds between carbon atoms within a graphite layers are considered to break when the distance between them is larger than a critical value. The sp³ bonds across the neighboring graphite layers form when the distance between them falls below a threshold. Such a treatment is efficient for qualitatively capturing the atomistic process of a graphite-to-diamond PT. However, it is purely empirical without the quantum-level accuracy for the real chemical bond breaking and formation. This might be one reason why diamonds are formed through the PTs in graphite under an unreasonably high compressive stress at a level of hundreds of GPa. In particular, the graphite-todiamond PT pressure measured from the present simulations is nearly one order higher than that (~30 GPa) from the simulations using an ab initio quality neuron network potential.³⁶ To check the dependence of the PT pressure on the interatomic potentials, we also recently performed a series of similar atomistic simulations using a reactive force field (ReaxFF),⁵¹ which is believed to able to retain the quantum mechanical accuracy for chemical bond breaking, switching, and formations, but demands significantly less computational cost than that by ab initio calculations. We found that the critical stress required for the PT in graphite using ReaxFF is largely reduced. Secondly, the atomistic models in this work are only for single-crystalline graphite. However, in real situations, microstructure of the graphite used for artificial diamond synthesis is extremely complicated. It contains a variety of different types of defects, such vacancies, interstitials, dislocations, grain boundaries, and chemical impurities, among many others, none of which are considered here but definitely play very important roles in PTs. As such, many quantitative measurements in this work, such as the critical compressive stress or strain for PTs, actually only provide an "upper bound" in an idealized situation. And, thirdly, when dislocations and PTs occur simultaneously, both of them will largely deviate the perfect crystal structure and introduce long-range stress fields into the materials. The effects of such heterogeneous stress fields could

span several microns and even above. This casts doubt on the quantitative prediction using MD for such a phenomenon, because the solution could be easily polluted by the image stresses no matter the free surface or the periodic boundary conditions are applied.

Hence, the incorporation of the complete microstructure complexity, as well as the full suite of mechanisms responsible for the dislocations, PTs and their interactions in graphite, necessitates a multiscale method that can link the atomic-scale processes to its deformation behavior at the micrometer level. Here, we argue that our recent concurrent atomisticcontinuum (CAC) method^{61–70} is such a strategy. Fundamental to CAC is a formulation that unifies atomistic and continuum descriptions of the materials. ⁷¹ This formulation generalizes Kirkwood's statistical theory of transport processes 72-75 by including a two-level description of crystals. It considers the crystalline material as a collection of continuously distributed lattice cells, within each of which a group of atoms is embedded. The atomic displacement field is then expressed as the sum of a continuum-level lattice deformation and a discrete sub-lattice internal deformation. This two-level description leads to governing equations that can be used to solve for the lattice cell deformation at a continuum level and also the internal motion of atoms at the sub-lattice level. 61,65 Thus. continuum modeling techniques, such as FE, can be used to solve it. The utilization of FE in regions where materials deform cooperatively leads to a coarsegrained (CG) model, ^{61,65} in which the atomic displacement is constrained using FE shape functions to reduce the number of degrees-of-freedom. For modeling dislocations or PTs, an element that conforms to the geometry of a material's primitive cell was adopted, e.g., a rhombohedral element for fcc crystals and silicon, in.^{61,65} One unique feature of CG is its capability of explicitly accommodating PTs,⁶¹ dislocation nucleation and migrations in a continuum domain at a fraction of the cost of MD, but without smearing out its atomistic nature. 61 The combination of the CG and atomistic model naturally leads to a unique multiscale materials modeling platform for predicting the complex dynamics of dislocations, PTs, and their interactions in materials from the atomistic to the micrometer level. The research of expanding the CAC computational framework for simulating the mechanical behavior in graphite under deformation will be intensively pursued and reported in our future work.

ACKNOWLEDGMENTS

We acknowledge the support of NSF (Grant No. CMMI-1536925 and CMMI-1824840) and the Extreme Science and Engineering Discovery Environment (TG-MSS170003).

REFERENCES

- 1. F. Bundy, J. Chem. Phys. 38, 631 (1963).
- R.M. Hazen, The diamond makers (Cambridge: Cambridge University Press, 1999).

Atomistic Computational Analysis of the Loading Orientation-Dependent Phase Transformation in Graphite under Compression

- 3. H.T. Hall, Science 128, 445 (1958).
- 4. M.G. Loshak and L.I. Alexandrova, Int. J. Refract. Met. Hard Mater. 19, 5 (2001).
- Y. Gao, Y. Ma, Q. An, V. Levitas, Y. Zhang, B. Feng, J. Chaudhuri, and W.A. Goddard, *Carbon* 146, 364 (2019).
- K. Edalati, T. Daio, Y. Ikoma, M. Arita, and Z. Horita, Appl. Phys. Lett. 103, 034108 (2013).
- W.L. Mao, H. Mao, P.J. Eng, T.P. Trainor, M. Newville, C. Kao, D.L. Heinz, J. Shu, Y. Meng, and R.J. Hemley, *Science* 302, 425 (2003).
- 8. Q. Li, Y. Ma, A.R. Oganov, H. Wang, H. Wang, Y. Xu, T. Cui, H.-K. Mao, and G. Zou, *Phys. Rev. Lett.* 102, 175506 (2009).
- 9. K. Umemoto, R.M. Wentzcovitch, S. Saito, and T. Miyake, *Phys. Rev. Lett.* 104, 125504 (2010).
- J.-T. Wang, C. Chen, and Y. Kawazoe, *Phys. Rev. Lett.* 106, 075501 (2011).
- H. Niu, X.-Q. Chen, S. Wang, D. Li, W.L. Mao, and Y. Li, Phys. Rev. Lett. 108, 135501 (2012).
- J.-T. Wang, C. Chen, and Y. Kawazoe, J. Chem. Phys. 137, 024502 (2012).
- M. Akaishi, H. Kanda, and S. Yamaoka, Jpn. J. Appl. Phys. 29, L1172 (1990).
- M. Akaishi, H. Kanda, and S. Yamaoka, J. Cryst. Growth 104, 578 (1990).
- 15. B. Feng, V.I. Levitas, and Y. Ma, *J. Appl. Phys.* 115, 163509
- 16. B. Feng and V.I. Levitas, *J. Appl. Phys.* 114, 213514 (2013).
- V.I. Levitas and O.M. Zarechnyy, *Phys. Rev. B* 82, 174123 (2010).
- B. Feng, V.I. Levitas, and W. Li, Int. J. Plast 113, 236 (2019).
- 19. V.I. Levitas and M. Javanbakht, Nanoscale 6, 162 (2014).
- 20. L.-Q. Chen, Annu. Rev. Mater. Res. 32, 113 (2002).
- 21. J.A. Warren and W.J. Boettinger, *Acta Metall. Mater.* 43, 689 (1995)
- M.A. Zaeem, N. Zhang, and M. Mamivand, Comput. Mater. Sci. 160, 120 (2019).
- S. Xu, J. R. Mianroodi, A. Hunter, I. J. Beyerlein, and B. Svendsen, *Philos. Mag.* 1 (2019).
- J. Mayeur, I. Beyerlein, C. Bronkhorst, and H. Mourad, *Int. J. Plast* 65, 206 (2015).
- J.R. Mayeur, D.L. McDowell, and D.J. Bammann, J. Mech. Phys. Solids 59, 398 (2011).
- M. Anahid, M.K. Samal, and S. Ghosh, J. Mech. Phys. Solids 59, 2157 (2011).
- Y. Hong, N. Zhang, and L. Xiong, J. Micromechanics Mol. Phys. 1, 1640007 (2016).
- 28. N. Zhang et al., J. Appl. Phys. 109, 063534 (2011).
- 29. N. Zhang and M.A. Zaeem, Acta Mater. 120, 337 (2016).
- V.I. Levitas, H. Chen, and L. Xiong, *Phys. Rev. B* 96, 054118 (2017).
- V.I. Levitas, H. Chen, and L. Xiong, *Phys. Rev. Lett.* 118, 025701 (2017).
- H. Chen, V. Levitas, and L. Xiong, Comput. Mater. Sci. 157, 132 (2019).
- M. Barsoum, X. Zhao, S. Shanazarov, A. Romanchuk, S. Koumlis, S. Pagano, L. Lamberson, and G. Tucker, *Phys. Rev. Mater.* 3, 013602 (2019).
- D. Freiberg, M. Barsoum, and G. Tucker, *Phys. Rev. Mater.* 2, 053602 (2018).
- 35. M. Barsoum and G. Tucker, Scr. Mater. 139, 166 (2017).
- R.Z. Khaliullin, H. Eshet, T.D. Kühne, J. Behler, and M. Parrinello, Nat. Mater. 10, 693 (2011).
- H. Xie, F. Yin, T. Yu, J.-T. Wang, and C. Liang, Sci. Rep. 4, 5930 (2014).
- M. Barsoum, A. Murugaiah, S. Kalidindi, T. Zhen, and Y. Gogotsi, Carbon 42, 1435 (2004).

- J. Gruber, A.C. Lang, J. Griggs, M.L. Taheri, G.J. Tucker, and M.W. Barsoum, Sci. Rep. 6, 33451 (2016).
- 40. S. Plimpton, 42 (n.d.).
- 41. Y. Chen and E.P.L. Europhys, Lett. 116, 34003 (2016).
- 42. Y. Chen and A. Diaz, Phys. Rev. E 98, 052113 (2018).
- J. Rigelesaiyin, A. Diaz, W. Li, L. Xiong, and Y. Chen, Proc. R. Soc. Math. Phys. Eng. Sci. 474, 20180155 (2018).
- 44. Y. Chen and A. Diaz, Phys. Rev. E 94, 053309 (2016).
- L.M. Ghiringhelli, J.H. Los, E.J. Meijer, A. Fasolino, and D. Frenkel, *Phys. Rev. Lett.* 94, 145701 (2005).
- L. Pastewka, A. Klemenz, P. Gumbsch, and M. Moseler, Phys. Rev. B 87, 205410 (2013).
- 47. J. Titantah and D. Lamoen, Carbon 43, 1311 (2005).
- 48. J. Tersoff, Phys. Rev. Lett. 61, 2879 (1988).
- M.J. López, I. Cabria, and J.A. Alonso, J. Chem. Phys. 135, 104706 (2011).
- G.-D. Lee, C. Wang, E. Yoon, N.-M. Hwang, D.-Y. Kim, and K. Ho, *Phys. Rev. Lett.* 95, 205501 (2005).
- P. Thrower and R. Mayer, Phys. Status Solidi A 47, 11 (1978).
- T. Liang, T.-R. Shan, Y.-T. Cheng, B.D. Devine, M. Noordhoek, Y. Li, Z. Lu, S.R. Phillpot, and S.B. Sinnott, *Mater. Sci. Eng. R Rep.* 74, 255 (2013).
- S.G. Srinivasan, A.C. Van Duin, and P. Ganesh, *J. Phys. Chem. A* 119, 571 (2015).
- 54. M.L. Falk and J.S. Langer, Phys. Rev. E 57, 7192 (1998).
- F. Shimizu, S. Ogata, and J. Li, *Mater. Trans.* 48, 2923 (2007).
- A.C. Van Duin, S. Dasgupta, F. Lorant, and W.A. Goddard, J. Phys. Chem. A 105, 9396 (2001).
- 57. A. Karma, Phys. Rev. Lett. 87, 115701 (2001).
- A. Stukowski, Model. Simul. Mater. Sci. Eng. 18, 015012 (2009).
- E. Maras, O. Trushin, A. Stukowski, T. Ala-Nissila, and H. Jonsson, Comput. Phys. Commun. 205, 13 (2016).
- 60. Y.X. Zhao and I.L. Spain, Phys. Rev. B 40, 993 (1989).
- L. Xiong, G. Tucker, D.L. McDowell, and Y. Chen, *J. Mech. Phys. Solids* 59, 160 (2011).
- L. Xiong, Q. Deng, G. Tucker, D.L. McDowell, and Y. Chen, *Acta Mater.* 60, 899 (2012).
- 63. L. Xiong, D.L. McDowell, and Y. Chen, Scr. Mater. 67, 633 (2012).
- H. Chen, S. Xu, W. Li, R. Ji, T. Phan, and L. Xiong, Comput. Mater. Sci. 144, 1 (2018).
- L. Xiong and Y. Chen, Model. Simul. Mater. Sci. Eng. 17, 035002 (2009).
- L. Xiong, D.L. McDowell, and Y. Chen, Int. J. Plast 55, 268 (2014).
- L. Xiong, X. Chen, N. Zhang, D.L. McDowell, and Y. Chen, Arch. Appl. Mech. 84, 1665 (2014).
- S. Xu, L. Xiong, Y. Chen, and D.L. McDowell, Acta Mater. 122, 412 (2017).
- S. Xu, L. Xiong, Y. Chen, and D.L. McDowell, J. Mech. Phys. Solids 96, 460 (2016).
- X. Chen, W. Li, L. Xiong, Y. Li, S. Yang, Z. Zheng, D.L. McDowell, and Y. Chen, *Acta Mater.* 136, 355 (2017).
- 71. Y. Chen, J. Chem. Phys. 130, 134706 (2009).
- 72. J.G. Kirkwood, J. Chem. Phys. 14, 180 (1946).
- 73. J.G. Kirkwood, J. Chem. Phys. 15, 72 (1947).
- R.J. Bearman and J.G. Kirkwood, J. Chem. Phys. 28, 136 (1958).
- 75. J. Irving and J.G. Kirkwood, J. Chem. Phys. 18, 817 (1950).

Publisher's Note Springer Nature remains neutral with regard to jurisdictional claims in published maps and institutional affiliations.